

Direct Chemical Vapor Deposition Synthesis of Porous Single-Layer Graphene Membranes with High Gas Permeances and Selectivities

Zhe Yuan, Guangwei He, Samuel Faucher, Matthias Kuehne, Sylvia Xin Li, Daniel Blankschtein, and Michael S. Strano*

Single-layer graphene containing molecular-sized in-plane pores is regarded as a promising membrane material for high-performance gas separations due to its atomic thickness and low gas transport resistance. However, typical etching-based pore generation methods cannot decouple pore nucleation and pore growth, resulting in a trade-off between high areal pore density and high selectivity. In contrast, intrinsic pores in graphene formed during chemical vapor deposition are not created by etching. Therefore, intrinsically porous graphene can exhibit high pore density while maintaining its gas selectivity. In this work, the density of intrinsic graphene pores is systematically controlled for the first time, while appropriate pore sizes for gas sieving are precisely maintained. As a result, single-layer graphene membranes with the highest H_2/CH_4 separation performances recorded to date (H_2 permeance > 4000 GPU and H_2/CH_4 selectivity > 2000) are fabricated by manipulating growth temperature, precursor concentration, and non-covalent decoration of the graphene surface. Moreover, it is identified that nanoscale molecular fouling of the graphene surface during gas separation where graphene pores are partially blocked by hydrocarbon contaminants under experimental conditions, controls both selectivity and temperature dependent permeance. Overall, the direct synthesis of porous single-layer graphene exploits its tremendous potential as high-performance gas-sieving membranes.


yield orders of magnitude higher gas permeances because of its atomic thickness and low cross-membrane transport resistance.^[3,4] Because perfect single-layer graphene is almost impermeable to gases,^[5,6] in-plane pores, which are vacancy defects in the graphene lattice, are necessary for gas permeation. To realize the enormous potential of porous graphene for gas separation, the areal pore density in graphene should be considerably high. Our group theoretically predicted that the pore density needs to exceed 10^{14} m^{-2} for a graphene membrane to surpass the Robeson upper bound for polymers.^[7,8] Further, to enable selective gas transport, the pore sizes in the graphene membrane should be precisely controlled such that they are commensurate with the gas molecular sizes. In fact, the pore sizes in porous graphene are typically widely distributed and fitted by a lognormal distribution, where a small fraction of larger pores determine the total gas permeance.^[9–12] As a result, an even higher pore density is needed for porous graphene to achieve a high gas permeance with enough competitiveness.

1. Introduction

Membrane separation technology has attracted considerable interest due to its much lower energy consumption compared with thermal-based separation methods such as distillation.^[1,2] To enhance the competitiveness of membrane separation processes, membranes exhibiting both high permeance and selectivity are in high demand. Compared with conventional membrane materials, single-layer graphene has the potential to

Etching away atoms from pristine graphene has been the most widely applied strategy to increase the pore density in a graphene membrane. High-energy ion or electron bombardment was used to perforate graphene in some early studies.^[12–15] Later, chemical oxidative etching was developed as a more scalable graphene perforation method.^[16–18] For example, He et al. used O_2 plasma to perforate as-synthesized graphene from chemical vapor deposition (CVD) and measured a H_2/CH_4 selectivity > 15.^[11] Zhao et al. exposed pristine graphene to O_2 plasma for a short pore nucleation burst, and then to mild O_3 etching for controllable pore expansion, in order to partially decouple the pore nucleation and growth and to obtain a narrow pore size distribution.^[19] However, despite the efforts made to decouple the pore nucleation and growth, the correlation between them still exists for those etching-based methods. Because the nucleation and growth of the pores are both triggered by etching (e.g., O_2 plasma), one needs to raise the energy intensity of the etching reaction to increase the pore density, which in turn generates larger, less selective pores. This

Z. Yuan, G. He, S. Faucher, M. Kuehne, S. X. Li, D. Blankschtein, M. S. Strano
Department of Chemical Engineering
Massachusetts Institute of Technology
Cambridge, MA 02139, USA
E-mail: strano@mit.edu

 The ORCID identification number(s) for the author(s) of this article can be found under <https://doi.org/10.1002/adma.202104308>.

DOI: 10.1002/adma.202104308

trade-off between the pore density and the selectivity remains a major challenge for graphene membranes.

A promising way to tackle this challenge is to control the formation of intrinsic pores in graphene during its CVD synthesis.^[20] According to the theoretical study by Wang et al., the formation of the intrinsic pores during CVD is triggered by the random insertion of catalytic metal atoms into the front-most graphene edge during growth,^[21] which is decoupled from oxidative etching. Therefore, the density of these intrinsic pores can be significantly increased without sacrificing their gas selectivity, as long as the density is not too high to induce pore coalescence. Several reported studies have investigated the gas separation performances of these intrinsic pores.^[22–26] However, the precise control over the density and the sizes of the intrinsic pores has not been realized, resulting in unsatisfactory permeances and selectivities.

In this study, for the first time, we systematically investigate the formation mechanism of the graphene pores that are intrinsically formed during CVD, and systematically control the density of the intrinsic pores by tuning the CVD synthesis conditions. This can be done without significantly increasing the pore sizes. This is important because it allows graphene membranes to present higher gas fluxes while maintaining high selectivities. Further, we demonstrate that the sizes of these intrinsic pores can be effectively modulated by manipulating the hydrocarbon adsorbates that partially block the pores. Using the strategies above, we reproducibly fabricated

single-layer graphene membranes exhibiting high densities of intrinsic gas-sieving pores that exhibit record-high H₂/CH₄ separation performances to date: H₂/CH₄ selectivity > 2000 while H₂ permeance > 4000 GPU (gas permeation unit, 1 GPU = 3.35 × 10^{−10} mol s^{−1} m^{−2} Pa^{−1}), or H₂/CH₄ selectivity > 100 while H₂ permeance > 10⁴ GPU.

2. Results and Discussion

2.1. Formation of Intrinsic Graphene Pores

Porous single-layer graphene was synthesized by one-step CVD using Cu as the catalyst and CH₄ as the precursor (see Experimental Section for details).^[27] Figure 1a shows the positive correlation between the CH₄ partial pressure $P(\text{CH}_4)$ during graphene growth and the D to G peak intensity ratio (I_D/I_G) of graphene measured by Raman spectroscopy. Corresponding Raman spectra are presented in Figure 1b. According to the amorphization trajectory of graphene, I_D/I_G is a non-monotonic function of the areal defect density ρ —it reaches a maximum when the average defect distance L_D ($= \rho^{-1/2}$) is ≈ 3 nm.^[28,29] The high 2D peaks shown in Figure 1b indicate that the defects are sparse ($L_D > 3$ nm).^[28] In this range, I_D/I_G is approximately proportional to the defect density ρ .^[29] This positive correlation between $P(\text{CH}_4)$ and ρ can be explained by the mechanism proposed by Wang et al. as follows.^[21] After a defect forms at

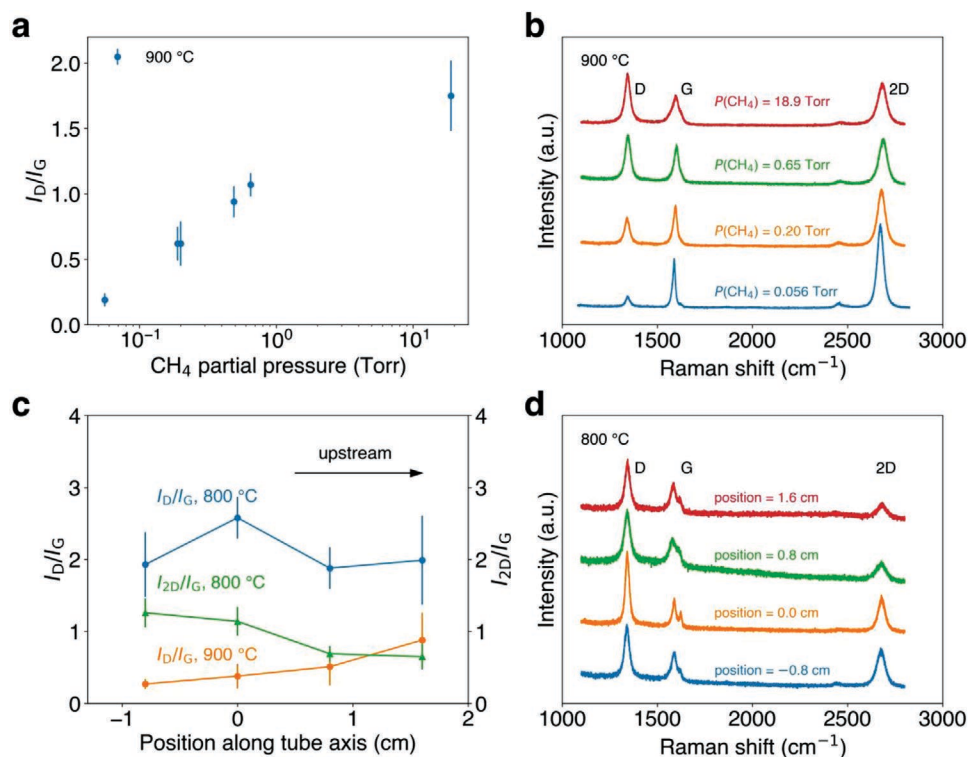


Figure 1. a) D to G peak intensity ratio (I_D/I_G) of CVD graphene's Raman spectrum as a function of CH₄ partial pressure during CVD at 900 °C. b) Raman spectra of CVD graphene samples grown with various CH₄ partial pressures at 900 °C. c) I_D/I_G (left y axis) and 2D to G peak intensity ratio (I_{2D}/I_G , right y axis) of CVD graphene as functions of position in the CVD heating zone along the CVD tube axis. Position = 0 stands for the center of the heating zone. d) Raman spectra of CVD graphene samples grown at 800 °C at different positions. The CH₄ partial pressure is 0.018 Torr for (c) and (d). The Raman excitation wavelength is 532 nm.

the front-most graphene edge during growth, it can be healed before the front-most edge extends and moves past it. Otherwise, the defect gets “frozen” inside the lattice and cannot be healed.^[30] As a result, when $P(\text{CH}_4)$ is high, the graphene growth is fast, leading to less time for the defects to be healed and subsequently, to a high defect density.^[31–33]

Figure 1c demonstrates the effect of CVD temperature on the density of the intrinsic defects, where I_D/I_G is larger for graphene grown at 800 °C (blue) than for that grown at 900 °C (orange). According to *ab initio* calculations, the defect formation energy at the front-most graphene edge is 1.3 eV, while the energy barrier associated with defect healing is 1.86 eV.^[21] Therefore, although a lower CVD temperature reduces the probability of defect formation, it reduces the probability of defect healing to a greater extent, resulting in a higher defect density. Similar temperature dependence was observed by Kidambi et al.^[34] and Khan et al.,^[25] but its mechanism has not been unveiled.

Figure 1c also presents the effect of a typically hidden CVD parameter—the position inside the heating zone. Ideally, the defect density should be nearly independent of the position. However, the density the intrinsic defects is spatially heterogeneous on the same Cu substrate from the same growth batch. More specifically, the defect density monotonically increases as the sample moves upstream. For example, I_D/I_G of CVD graphene grown at 900 °C (orange) increases as the position along CVD tube axis moves upstream from −0.8 to 1.6 cm relative to the heating zone center. The defect density of the graphene sample grown at 900 °C is low (Figure S1, Supporting Information), and therefore, is positively correlated with I_D/I_G , according to the amorphization trajectory of graphene when $L_D > 3$ nm. In contrast, I_D/I_G of CVD graphene grown at 800 °C (blue) first increases and then decreases while moving upstream. This is because L_D reaches the maximum point of the amorphization trajectory at ≈ 3 nm. The monotonically decreasing I_{2D}/I_G moving upstream (green curve in Figure 1c,d) indicates that the defect density increases.^[29] This consistent spatial heterogeneity in defect density indicates the existence of a spatially variable parameter along the CVD tube axis.

We hypothesize that the parameter is the concentration of O_2 from an air leak (see Section S2, Supporting Information, for more details about ruling out other possibilities). O_2 is known to significantly affect the CVD growth of graphene, even at a low concentration.^[35–38] For a CVD system operated under vacuum, an air leak is difficult to be eliminated, and O_2 is the only major reactive component in air. In order to identify the source of the air leak (upstream or downstream), we artificially increased the air leak by using a pair of leakier O-rings to seal the connection between the CVD quartz tube and the metal flanges. The increased air leak led to a decrease in defect density (Figure S2, Supporting Information). Therefore, we: i) confirmed the effect of O_2 on the graphene defect density, and ii) confirmed that the correlation between the O_2 concentration and the defect density is negative. Note that in this work, O_2 does not cause defect nucleation. Instead, O_2 inhibits defect nucleation by reducing the graphene growth rate, because O_2 can react with graphene edges or active carbon species.^[39] Because the defect density was found to monotonically increase from downstream to upstream, the O_2 concentration should

monotonically decrease from downstream to upstream, which indicates a major air leak source from the downstream pipeline, most likely, the vacuum pump (see Section S2, Supporting Information, for more discussions). We believe this finding is important because the unnoticed difference in air leak conditions among laboratories might have caused the low reproducibility of graphene CVD synthesis.

An alternative hypothesis of the intrinsic defects is that they are solely formed at grain boundaries due to imperfect merging.^[40,41] We have ruled out this hypothesis because consistent $I_D/I_G > 0$ can be observed inside a single graphene crystal (Figure S3, Supporting Information). Furthermore, we have confirmed that the graphene defects are mainly vacancies instead of sp^3 -like defects or boundary defects because the D to D' peak intensity ratio ($I_D/I_{D'}$) of our CVD graphene is 8.2 ± 0.2 (Figure S4, Supporting Information), consistent with the study by Eckmann et al. ($I_D/I_{D'} \approx 7$ for vacancies, ≈ 3.5 for boundary defects, and ≈ 13 for sp^3 -like defects).^[42] Therefore, the majority of the defects in our graphene membranes are vacancies, which are regarded as in-plane pores.

2.2. Gas Separation Performances

After synthesizing a continuous single-layer graphene film with intrinsic pores on Cu, we transferred the graphene onto a Ni disk with a 100×100 array of 4.2 ± 0.3 - μm -diameter holes (Figure 2a,b). In order to prevent graphene rupture, we utilized a porous carbon scaffold (PCS) as mechanical support (see Experimental Section for details).^[23,43] The PCS ensures that the graphene membrane remains intact on the hole-array (Figure 2c). The enhanced graphene membrane remained intact after several weeks' testing. Furthermore, its gas permeances remained nearly the same after two month's storage in a petri dish. The carbon scaffold is highly permeable (Table S1, Supporting Information), such that the gas permeance through the porous carbon/graphene composite membrane is dominated by the graphene layer (Figure 2d).^[19,23]

After graphene synthesis and membrane transfer, the graphene membranes suspended over the hole-array were tested for their H_2 , He, CH_4 , and SF_6 permeances using a mass spectrometer. Because the mass spectrometer is not sensitive to H_2 , the H_2 permeance data of some membranes exhibit high uncertainty (Figure S13c, Supporting Information). As a solution, we used He as the representative for small gas molecules (kinetic diameter $D_m = 0.26$ nm),^[44] because i) its signal was higher and more stable, ii) the H_2/He selectivity was ≈ 1.4 for all the membranes investigated, close to the Knudsen selectivity for effusion-type gas transport (Table S1, Supporting Information), and iii) He/ CH_4 separation is essential for helium recovery from natural gas.^[45,46]

Figure 3a,b show the He/ CH_4 and He/ SF_6 separation performances of the graphene membranes. Datapoints of the same color represent the same membrane measured under different conditions, including temperature, surface decoration, and air exposure. The graphene membranes were classified into four color families, red, orange, green, and blue, corresponding to four different CVD parameter sets. Comparing the blue family (900 °C, $P(\text{CH}_4) = 0.19$ Torr) to the green family

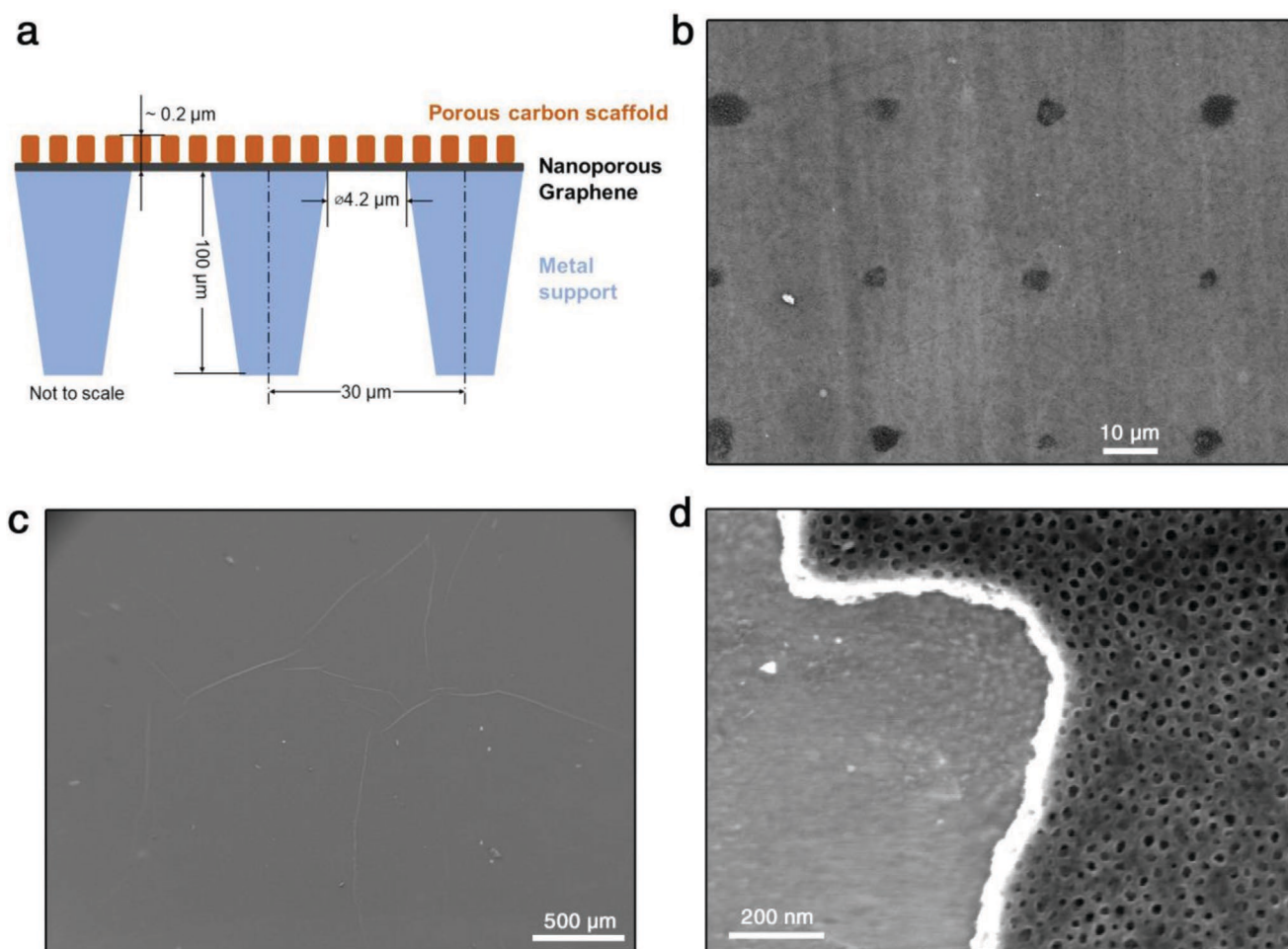


Figure 2. a) Schematic of the final membrane (not to scale). Scanning electron microscopy (SEM) images of a single-layer graphene membrane supported by a porous carbon scaffold on a 100×100 hole-array, using accelerating voltages of b) 7 kV and c) 2 kV, respectively. (b) shows a zoomed-in image and (c) shows that the membrane is intact. d) SEM image of a top view of the edge of the porous carbon scaffold.

(1000°C , $P(\text{CH}_4) = 0.19$ Torr), or the red family (800°C , $P(\text{CH}_4) = 0.018$ Torr) to the orange family (900°C , $P(\text{CH}_4) = 0.018$ Torr), we observed that a lower CVD temperature yields higher He permeances because of the higher pore density (Figure 1c). Further, a lower CVD temperature does not lead to a significant decrease in selectivity. The effect of $P(\text{CH}_4)$ is different. Compared to the orange family ($P(\text{CH}_4) = 0.018$ Torr, 900°C), the blue family ($P(\text{CH}_4) = 0.19$ Torr, 900°C) exhibits higher He permeances but also lower selectivities. The observed selectivity decrease for high $P(\text{CH}_4)$ can be attributed to the coalescence of overly dense intrinsic pores into larger ones, thereby reducing the selectivity. In Figure 3a, several top-left datapoints with long dashed error bar upward indicate the lower bound of He/ CH_4 selectivities, because their CH_4 signals were below the detection limit (Section S8, Supporting Information).

The position of graphene inside the CVD heating zone also plays a major role. Within each color family, datapoints of deeper color represent a membrane sample closer to the upstream (legend in Figure 3a,b; also see Figure S5, Supporting Information). For example, in the orange family in Figure 3a,b, the membrane position moves upstream from the light yellow to the orange, and then to the brown circles.

Generally, the upstream membranes exhibit higher selectivities compared to the downstream ones while exhibiting similar He permeances, making moving a graphene sample upstream in the CVD heating zone a simple and reliable strategy to improve its membrane performance. This trend suggests that the upstream membranes have smaller pore sizes as well as higher pore densities. This further strengthens the hypothesis that the spatial heterogeneity of intrinsic graphene pores was caused by the gradient of O_2 concentration. Here, O_2 serves as an etchant that expands graphene pores.^[39,48,49] The monotonic decrease of O_2 concentration from downstream to upstream was consistent with the pore size decrease in the same direction. Note that O_2 has a dual effect on the intrinsic graphene pores: O_2 inhibits the nucleation of the intrinsic pores, but also expands the pores that survive the defect healing process (see Section S3, Supporting Information, for more discussions). Therefore, a low O_2 concentration is beneficial for both gas permeance and selectivity. Note that membrane ID = 17 was synthesized one month later than membrane ID = 10. This consistency indicates that our fabrication method of porous graphene was robust enough to withstand random external fluctuations.

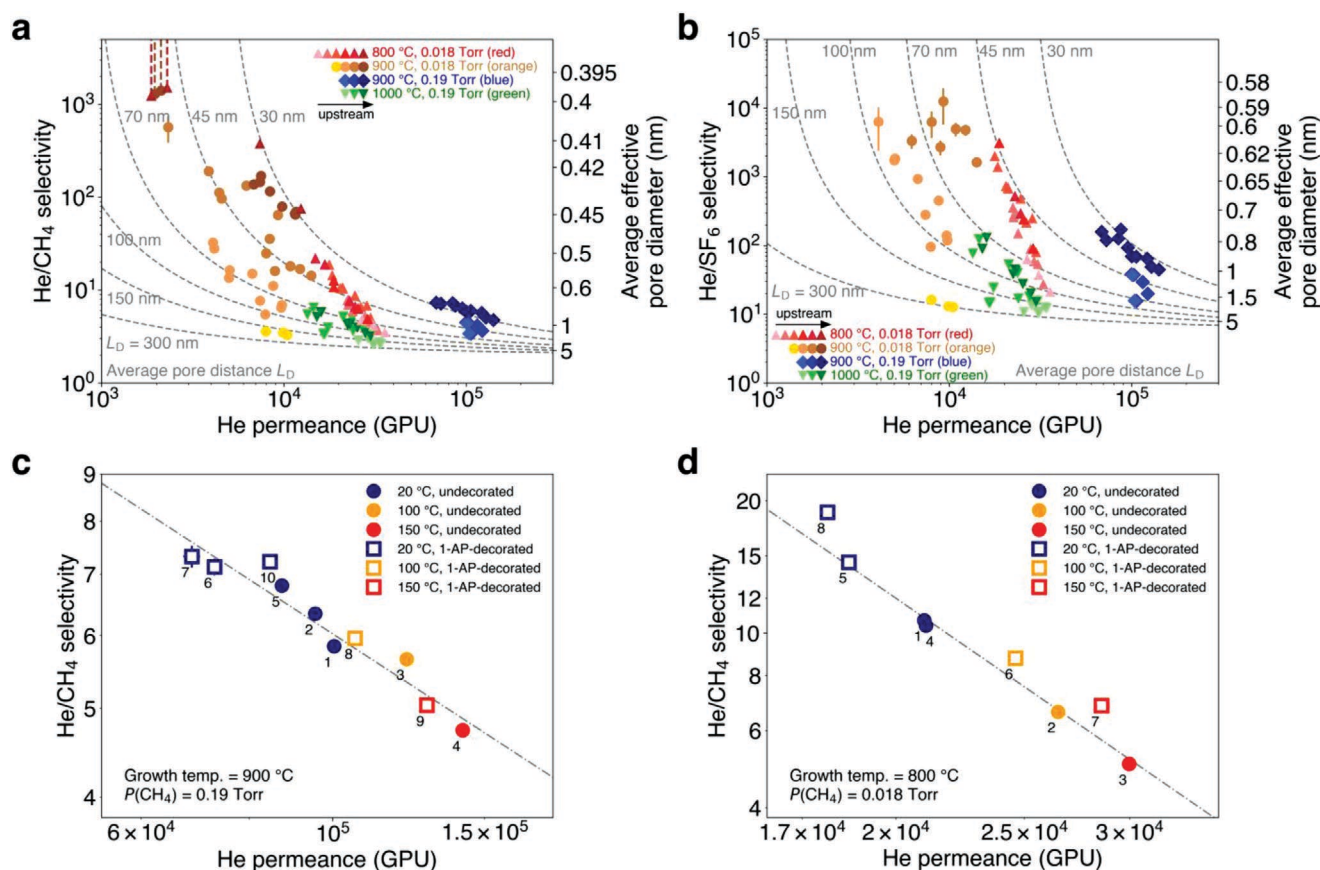


Figure 3. a) He/CH₄ selectivities and He permeances of graphene membranes. Datapoints of the same color represent the same membrane under different conditions (temperature, surface decoration, etc.). Top-left datapoints with long dashed error bar upward indicate the lower bound of He/CH₄ selectivities, because CH₄ signals were below the detection limit. Dashed grey curves indicate the theoretically predicted selectivity-permeance trade-off curves for various pore densities (iso-pore-density trade-off curves).^[47] Right y axis presents the theoretically predicted average effective pore diameter that corresponds to the left y axis. b) He/SF₆ selectivities and He permeances of graphene membranes. Other details are the same as in (a). c,d) He/CH₄ separation performance history of two graphene membranes, tested at different temperatures and surface decoration states. The numbers below the datapoints represent the testing sequence. 1-AP indicates 1-aminopyrene.

2.3. Iso-Pore-Density Trade-Off Curves

After evaluating the effects of the CVD parameters (temperature, CH₄ partial pressure, and sample position), in this subsection, we examine how the gas separation property of the same graphene membrane depends on the condition of permeation measurement. The effects of measurement temperature and surface decoration are illustrated in Figure 3c,d, where the selectivity-permeance trade-off of two individual graphene membranes are presented. Figure 3c corresponds to the deep blue datapoints in Figure 3a, and Figure 3d corresponds to the red datapoints. Regarding Figure 3c,d, we make the following observations. First, a higher measurement temperature yields a lower selectivity and a higher gas permeance. A plausible hypothesis is that the gas permeation is an activated process, and the energy barrier of pore crossing is positive.^[5,7] However, this hypothesis cannot explain the low and similar apparent energy barriers (derived by direct fitting to the Arrhenius equation) of He, CH₄, and SF₆ for some low-selectivity samples (see Sections S5, Supporting Information, for details). To resolve this inconsistency, we hypothesize that

under experimental conditions, graphene pores are partially blocked by airborne hydrocarbon contaminants adsorbed on graphene surfaces. As the temperature increases, the contaminants partially desorb, alleviating the pore blockage and effectively expanding the pore size. In our previous work, we fitted the theory of gas permeation through graphene pores to the data reported in the literature,^[11,19,25,26] and showed that the graphene pores have to effectively expand thermally to obtain a reasonable fitting.^[50] Further, Zhao et al. showed that annealing the graphene membrane at high temperature alleviates the contamination and increases the gas permeance.^[19] It has also been observed that the adsorption of airborne hydrocarbons on graphitic surfaces renders them more hydrophobic during water contact angle measurements.^[51,52] This contamination hypothesis also explains the observed shift from datapoint 1 to 2 in Figure 3c resulting solely from exposing the membrane to air (the numbers below the datapoints represent the testing sequence).

The second observation from Figure 3c,d is that the non-covalent decoration of 1-aminopyrene (1-AP) on the graphene membranes leads to increased selectivity and reduced He

permeance (hollowed squares vs solid circles). 1-AP can strongly bind to the graphene surface due to strong π - π stacking, thereby enhancing pore blockage and effectively reducing the pore sizes. The effect of 1-pyrenebutyric acid (1-PBA) is almost identical to that of 1-AP, suggesting that pyrene plays the major role (membrane ID = 1 vs 2 in Table S1, Supporting Information). Furthermore, the temperature dependences of the selectivity and the permeance in Figure 3c,d are very similar before and after the 1-AP decoration. This strongly suggests that the undecorated graphene surface has already been covered by some pore-blocking adsorbates, which play a similar role as those of 1-AP or 1-PBA, albeit weaker in terms of pore blockage.

Based on the analysis above, we can attribute the selectivity-permeance trade-off curves observed in Figure 3c,d to the effective pore size change, which is induced by the status change of the pore-blocking contaminants, or the “nanoscale fouling.” Graphene membranes are susceptible to this nanoscale fouling effect because the gas transport resistance through graphene pores is dominated by the entrance/exit resistance at the surface.^[47] Assuming that the pore density of a graphene membrane remains constant during its testing history, hereafter, we refer to the selectivity-permeance trade-off curves as “iso-pore-density trade-off curves,” where moving along the curves reflects the changes in the effective pore size.

These iso-pore-density trade-off curves can also be observed for other graphene membranes, as shown in Figure 3a,b. Generally, at a higher selectivity, there are sharper changes in selectivity with small changes in permeance, indicating that smaller pores are more sensitive to the nanoscale fouling. To explain this trend, we carry out theoretical investigation as follows. According to the gas permeation mechanism through perfectly clean porous graphene,^[47] direct impingement from bulk gas, surface diffusion, and cross-pore translocation all affect the gas permeance. However, our nanoscale fouling hypothesis motivates us to consider solely the direct impingement permeance, the contribution that is not affected by the condition of the graphene surface. Therefore, the permeance of gas i through a graphene membrane can be predicted as follows, assuming uniform pore sizes:^[47]

$$K_i = \rho \times \frac{\pi D_p^2}{4} \times \frac{1}{\sqrt{2\pi m_i k_B T}} \times \left(1 - \frac{D_{m,i}}{D_p}\right)^{\alpha_i} \quad (1)$$

where ρ is the areal pore density, D_p is the effective pore diameter (after partial blockage by nanoscale fouling), m_i is the molecular weight of gas i , $D_{m,i}$ is the kinetic diameter of gas i , k_B is the Boltzmann constant, and T is the measurement temperature in degrees Kelvin. We assume that the graphene pores are circular because the most probable pore isomers generated in the graphene lattice are nearly circular.^[53] The $(1 - D_{m,i}/D_p)^{\alpha_i}$ term in Equation (1) describes the steric rejection effect due to the collision between gas i and the pore edges, and α_i is a gas i -dependent parameter which equals 3 if all gas-graphene interactions, other than collisions, can be neglected.^[47] According to Equation (1), the slope of the iso-pore-density trade-off curve (Figure 3c,d) can be expressed as follows (see Section S4, Supporting Information, for derivation):

$$-\text{Slope} = \frac{\frac{\alpha_2 D_{m,2}}{2} \frac{D_p - D_{m,1}}{D_{m,1}} - 1}{\frac{\alpha_1 D_{m,1}}{2} \frac{D_p - D_{m,2}}{D_{m,2}} + 1} \quad (2)$$

where $i = 1$ and 2 denote the more and the less permeable gas species, respectively. As shown in Equation (2), the slope of the iso-pore-density trade-off curve significantly increases (in absolute value) in a nonlinear manner as D_p approaches the kinetic diameter of the larger gas $D_{m,2}$. This nonlinearity is displayed by the right y axes in Figure 3a,b, where the predicted average effective pore diameter corresponding to the left y axes is plotted. As the average D_p approaches 0.38 or 0.55 nm (D_m of CH₄ and SF₆, respectively), the He/CH₄ or He/SF₆ selectivity significantly increases.

Assuming that the pore diameters in the graphene membranes follow lognormal distributions, which are widely observed in graphene pore ensembles,^[9,11] we attempted to fit the theoretical model to the experimental gas permeance data (see Section S4, Supporting Information, for details). The fitting predicts that the effective pore diameter shrinks by $(9 \pm 3)\%$ from 150 to 100 °C and shrinks by $(23 \pm 6)\%$ from 150 to 20 °C (Table S2, Supporting Information). Theoretically predicted iso-pore-density trade-off curves are plotted as the dashed curves in Figure 3a,b, where each curve corresponds to a certain pore density ρ (or L_D). The predicted iso-pore-density trade-off curves successfully reproduce the selectivity-permeance trade-off observed in Figure 3a,b. Note that the pore density estimated according to the iso-pore-density trade-off curves is typically lower than that estimated by I_D/I_G because i) the PCS blocks some membrane area, and ii) only a fraction of the pores contribute to gas permeation due to the pore size distribution. The applicability of Equation (1) to other datasets in the literature is discussed in Section S6, Supporting Information.

2.4. Comparison with the Literature

Figure 4 presents a comparison of the H₂/CH₄ separation performances of our intrinsically porous single-layer graphene membranes and other state-of-the-art membranes in the selectivity-permeance Robeson plot (see Figure S9, Supporting Information, for He/CH₄ Robeson plot). Some of the highest-performance graphene membranes in our study show H₂ permeance $> 10^4$ GPU and H₂/CH₄ selectivity > 100 , exceeding the Robeson upper bound for 1- μ m thick polymer membranes and the performances of some other materials.^[2,8,55–80] Some highly selective graphene membranes that we fabricated exhibit very low CH₄ permeances at room temperature such that their CH₄ signals are lower than the detection limit of the mass spectrometer, leading to extremely high H₂/CH₄ selectivities of at least 2000 (Section S8, Supporting Information). Meanwhile, they still exhibit decent H₂ permeances > 4000 GPU. If the iso-pore-density trade-off curves predicted in Figure 3 remains valid for these highly selective membranes, they can be regarded as nearly CH₄-impermeable. In comparison, the highest H₂/CH₄ selectivity obtained from a single-layer graphene membrane in previous studies was 375 (with H₂ permeance ≈ 7200 GPU), obtained recently by Huang et al.^[54] In general, the highest-performance

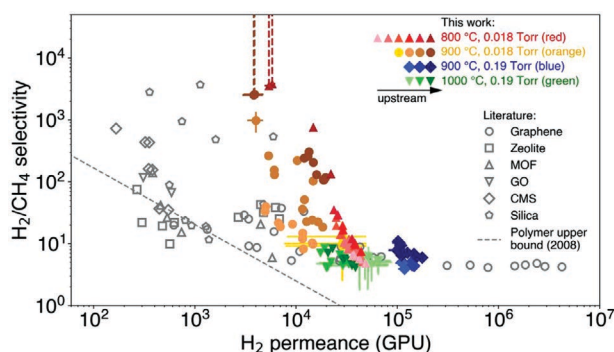


Figure 4. Selectivity-permeance Robeson plot of H_2/CH_4 separation. Results of this study are plotted as solid markers. Datapoints with long dashed error bar upward indicate the lower bound of H_2/CH_4 selectivities, because CH_4 signals were below the detection limit. Performances of other state-of-the-art membranes in the literature are plotted as hollow markers, including graphene,^[18,19,23,54] zeolite,^[55–60] metal-organic frameworks (MOF),^[61–66] graphene oxide (GO),^[67,68] carbon molecular sieves (CMS),^[69–72] silica,^[73–80] and Robeson upper bound for polymers assuming 1 μm thickness.^[8]

graphene membranes were synthesized under the following conditions: low CVD temperature (800 to 900 °C), $P(\text{CH}_4) = 0.018$ Torr, and upstream position in the CVD heating zone. These conditions contribute to the high membrane performance because i) the low CVD temperature generates more pores, ii) the appropriate $P(\text{CH}_4)$ prevents pore coalescence, and iii) the upstream position increases the pore density and reduces the pore sizes. Figure 4 demonstrates the advantage of single-layer graphene membranes for gas separations due to their atomic thickness and negligible interior gas transport resistance. This advantage is realized by effectively increasing the pore density while preserving small pore sizes, which relies on the effective control over the intrinsic pore formation during graphene CVD.

3. Conclusion

In summary, we demonstrated a strategy to synthesize single-layer graphene with a high density of gas-sieving pores using one-step CVD. By generating intrinsic graphene pores during CVD, we decoupled pore nucleation and growth. This allowed us to overcome the challenging trade-off between a high pore density and a high selectivity, which has been a key bottleneck for oxidative etching methods. We gained deep insight into the formation mechanism of the intrinsic graphene pores and substantially increased the pore density while maintaining precise pore sizes for gas separation. The resulting graphene membranes exhibit record-high gas separation performances to date, reaching H_2/CH_4 selectivity > 2000 while H_2 permeance > 4000 GPU, or H_2/CH_4 selectivity > 100 while H_2 permeance > 10^4 GPU. We also proposed the nanoscale fouling effect, where the graphene pores are partially blocked by hydrocarbon contaminants. This effect highlights the critical role of the adsorbed molecules near the pore edge in gas permeation. Overall, the straightforward one-step CVD approach represents an important advance toward the application of nanoporous graphene as high-performance gas separation membranes.

4. Experimental Section

Graphene Synthesis: Single-layer graphene was synthesized by CVD on a Cu foil (Sigma-Aldrich, 99.98% purity, 25 μm thick, 2.4 cm \times 1.6 cm in length and width) using CH_4 (diluted in H_2) as the precursor. Prior to CVD, the Cu foil was electropolished in an acidic electrolyte to reduce its surface roughness. The electrolyte was prepared by mixing water (400 mL), ethanol (200 mL), isopropanol (40 mL), orthophosphoric acid (200 mL), and urea (4 g) followed by stirring. A voltage of 6.0 V was applied between the cathode (Cu foil to be electropolished) and the anode (Cu foil) for 90 s, while the cathode and the anode were placed 2–3 cm apart. The electropolished Cu foil was rinsed with deionized water, ethanol, and isopropanol in sequence, dried under air flow, and placed inside the quartz tube (1" outer diameter) on a quartz boat (see Figure S11, Supporting Information, for a diagram of the CVD setup). A single-zone split tube furnace was used (MTI Corp., OTF-1200X-S). A pair of Quick Clamp Hi-Vacuum Flanges (MTI Corp.), along with a pair of high temperature silicone rubber O-rings (MTI Corp., QF-OR), were used to seal the connections between the quartz tube and the metal flanges. After sealing all immobile metal fittings using Torr Seal epoxy (K. J. Lesker), the minimum air leak rate was 5 mTorr L min^{−1} (excluding the vacuum pump). Before CVD growth, the Cu foil was annealed at the growth temperature (800–1000 °C) in 0.5 atm H_2 for 16 h while the H_2 flow rate was 70 sccm. During a growth period of 3 h (except for membrane ID = 16–18, 1 h), a certain flow rate of CH_4 (ranging from 0.1 to 3.0 sccm, depending on the desired CH_4 partial pressure) was fed, while the H_2 flow rate was 10 sccm. The chamber pressure during CVD growth was 1.5 Torr. The CVD chamber was evacuated by an oil-sealed rotary vacuum pump (Edwards RV12, ultimate pressure 1.5 mTorr, pumping speed 14.2 m³ h^{−1}) with its gas ballast closed. The pump oil was Edwards Ultragrade 19. A molecular sieve foreline trap (MDC Precision, 4.5" body, NW25) was connected to the vacuum pump to trap hydrocarbons and water. The CVD growth was terminated by stopping the CH_4 feed and shutting down the furnace. A trace oxygen analyzer (1–1000 ppm, EQ-W1000-LD, MTI Corp.) was sometimes connected to the quartz tube to measure the concentration of O_2 . The trace oxygen analyzer must be detached from the reactor during the CVD growth of graphene because the organic electrolyte in the analyzer would interfere with the CVD process.

Graphene Membrane Fabrication: The as-synthesized graphene/Cu sample was spin-coated (500 rpm, 1 min) with a solution of poly(styrene)-poly(4-vinylpyridine) (PS-P4VP, 0.1 g, Polymer Source, $M_n(\text{PS}) = 11\,800$ g mol^{−1}, $M_n(\text{P4VP}) = 12\,300$ g mol^{−1}, $M_w/M_n = 1.08$) and turanose (0.2 g, Sigma-Aldrich, $\geq 98\%$ purity) in *N,N*-dimethylmethanamide (2 g). The solution was heated at 150 °C for 16 h before use. The spin-coated graphene/Cu was then pyrolyzed at 460 °C in an H_2/Ar atmosphere for 1.5 h, forming the PCS adhering to graphene (≈ 200 nm thick, Figure S10, Supporting Information). Flat Cu surface is recommended during spin-coating. Otherwise, the thickness of the PCS would be uneven, causing the PCS to fracture. The PCS/graphene/Cu was cut into ≈ 0.8 cm \times ≈ 0.8 cm pieces, and the Cu foil of each piece was etched away by an aqueous solution of $\text{Na}_2\text{S}_2\text{O}_8$ (Transene Co.) for 2 h. After being rinsed twice with deionized water, the PCS/graphene composite was transferred by scooping onto a 100- μm -thick Ni disk with an array of 100 \times 100 laser-drilled 4.2 ± 0.3 - μm -diameter holes with a 30 μm pitch (Oxford Lasers). For some membranes, 50- μm -thick W disks with an array of 20 \times 20 laser-drilled holes were used. The membrane was dried at room temperature overnight. Non-covalent decoration of the graphene surface was carried out by submerging a graphene membrane into a 2 mmol L^{−1} solution of 1-aminopyrene (97%, Sigma-Aldrich) or 1-PBA (97%, Sigma-Aldrich) in ethanol. Subsequently, the graphene membrane was dried in the air for at least 30 min before gas permeation testing.

Gas Permeation Testing: The Ni disk carrying the graphene membrane was mounted into a homemade permeation module (Figure S12, Supporting Information). A gas mixture containing H_2 , He, CH_4 , and SF_6 was fed toward the membrane. The pressure difference for gas permeation was 1.0 bar. Permeated gases were swept by an Ar flow into a pre-calibrated mass spectrometer (Agilent 5977A with Diablo 5000A real

time gas analyzer). The permeances of the gases and their confidence intervals were calculated based on the mass spectroscopy signals collected in a 5-min duration after steady state was reached (Section S8, Supporting Information). Because graphene adhered to the Ni support could not contribute any gas flow,^[5] in this work, gas permeances were calculated based on the area of the laser-drilled holes (see Figure S8, Supporting Information, for permeances calculated based on the total area of the Ni support). The gas permeance from a pure feed was also measured, and was almost identical to that from a mixture feed (Figure S14, Supporting Information).

Membrane Characterization: Graphene membranes were imaged using a Zeiss Sigma 300 VP SEM operated at an accelerating voltage of 0.5–10 kV. Raman spectra of graphene samples were collected using a Horiba LabRAM micro-Raman spectrometer with a 532 nm excitation laser wavelength, 1800 grooves mm⁻¹ grating, and 50x objective. For Raman spectroscopy measurements, graphene samples were transferred onto a Si wafer using polymethyl methacrylate (PMMA)-assisted transfer, where the PMMA layer was removed by acetone. Each I_D/I_G data point in Figure 1a,c was the average over a mapping of 25 individual Raman spot measurements. The pitch between neighboring spots was 30 μm in the x direction, and 25 μm in the y direction. The laser spot diameter was $\approx 1 \mu\text{m}$.^[24]

Supporting Information

Supporting Information is available from the Wiley Online Library or from the author.

Acknowledgements

The authors acknowledge financial support from the National Science Foundation (NSF) grant number CBET-1907716. This work was supported as part of the Center for Enhanced Nanofluidic Transport (CENT), an Energy Frontier Research Center funded by the U.S. Department of Energy, Office of Science, Basic Energy Sciences under Award # DE-SC0019112. This work was also supported in part by the U.S. Army Research Laboratory (ARL) and the U.S. Army Research Office (ARO) through the Institute for Soldier Nanotechnologies (ISN), under contract number W911NF-13-D-0001. G.H. acknowledges the funding from Swiss National Science Foundation (Grant No. P400P2_186682). S.F. acknowledges support by the National Science Foundation Graduate Research Fellowship under Grant No. 1122374. M.K. acknowledges support by the German Research Foundation (DFG) Research Fellowship (Grant No. KU 3952/1-1).

Conflict of Interest

The authors declare no conflict of interest.

Data Availability Statement

The data that supports the findings of this study are available in the supplementary material of this article.

Keywords

chemical vapor deposition, gas separation, graphene membranes, graphene pores, single-layer graphene

Received: June 4, 2021

Revised: August 5, 2021

Published online: September 12, 2021

- [1] D. S. Sholl, R. P. Lively, *Nature* **2016**, 532, 435.
- [2] H. B. Park, J. Kamcev, L. M. Robeson, M. Elimelech, B. D. Freeman, *Science* **2017**, 356, eaab0530.
- [3] F. Zhou, M. Fathizadeh, M. Yu, *Annu. Rev. Chem. Biomol. Eng.* **2018**, 9, 17.
- [4] L. Wang, M. S. H. Boutilier, P. R. Kidambi, D. Jang, N. G. Hadjiconstantinou, R. Karnik, *Nat. Nanotechnol.* **2017**, 12, 509.
- [5] J. S. Bunch, S. S. Verbridge, J. S. Alden, A. M. van der Zande, J. M. Parpia, H. G. Craighead, P. L. McEuen, *Nano Lett.* **2008**, 8, 2458.
- [6] P. Z. Sun, Q. Yang, W. J. Kuang, Y. V. Stebunov, W. Q. Xiong, J. Yu, R. R. Nair, M. I. Katsnelson, S. J. Yuan, I. V. Grigorieva, M. Lozada-Hidalgo, F. C. Wang, A. K. Geim, *Nature* **2020**, 579, 229.
- [7] Z. Yuan, A. G. Rajan, R. P. Misra, L. W. Drahushuk, K. V. Agrawal, M. S. Strano, *ACS Nano* **2017**, 11, 7974.
- [8] L. M. Robeson, *J. Membr. Sci.* **2008**, 320, 390.
- [9] S. C. O'Hern, M. S. H. Boutilier, J.-C. Idrobo, Y. Song, J. Kong, T. Laoui, M. Atieh, R. Karnik, *Nano Lett.* **2014**, 14, 1234.
- [10] G. He, S. Huang, L. F. Villalobos, J. Zhao, M. Mensi, E. Oveisi, M. Rezaei, K. V. Agrawal, *Energy Environ. Sci.* **2019**, 12, 3305.
- [11] G. He, S. Huang, L. F. Villalobos, M. T. Vahdat, M. D. Guiver, J. Zhao, W.-C. Lee, M. Mensi, K. V. Agrawal, *Adv. Funct. Mater.* **2020**, 30, 2003979.
- [12] M. S. H. Boutilier, D. Jang, J.-C. Idrobo, P. R. Kidambi, N. G. Hadjiconstantinou, R. Karnik, *ACS Nano* **2017**, 11, 5726.
- [13] K. Celebi, J. Buchheim, R. M. Wyss, A. Droudian, P. Gasser, I. Shorubalko, J.-I. Kye, C. Lee, H. G. Park, *Science* **2014**, 344, 289.
- [14] M. S. H. Boutilier, N. G. Hadjiconstantinou, R. Karnik, *Nanotechnology* **2017**, 28, 184003.
- [15] C. J. Russo, J. A. Golovchenko, *Proc. Natl. Acad. Sci. USA* **2012**, 109, 5953.
- [16] S. P. Koenig, L. Wang, J. Pellegrino, J. S. Bunch, *Nat. Nanotechnol.* **2012**, 7, 728.
- [17] L. Wang, L. W. Drahushuk, L. Cantley, S. P. Koenig, X. Liu, J. Pellegrino, M. S. Strano, J. S. Bunch, *Nat. Nanotechnol.* **2015**, 10, 785.
- [18] K.-P. Schlichting, D. Poulikakos, *ACS Appl. Mater. Interfaces* **2020**, 12, 36468.
- [19] J. Zhao, G. He, S. Huang, L. F. Villalobos, M. Dakhchoune, H. Bassas, K. V. Agrawal, *Sci. Adv.* **2019**, 5, eaav1851.
- [20] F. Banhart, J. Kotakoski, A. V. Krashenninnikov, *ACS Nano* **2011**, 5, 26.
- [21] L. Wang, X. Zhang, H. L. W. Chan, F. Yan, F. Ding, *J. Am. Chem. Soc.* **2013**, 135, 4476.
- [22] M. S. H. Boutilier, C. Sun, S. C. O'Hern, H. Au, N. G. Hadjiconstantinou, R. Karnik, *ACS Nano* **2014**, 8, 841.
- [23] S. Huang, M. Dakhchoune, W. Luo, E. Oveisi, G. He, M. Rezaei, J. Zhao, D. T. L. Alexander, A. Züttel, M. S. Strano, K. V. Agrawal, *Nat. Commun.* **2018**, 9, 2632.
- [24] Z. Yuan, J. D. Benck, Y. Eatmon, D. Blankschtein, M. S. Strano, *Nano Lett.* **2018**, 18, 5057.
- [25] M. H. Khan, M. Moradi, M. Dakhchoune, M. Rezaei, S. Huang, J. Zhao, K. V. Agrawal, *Carbon* **2019**, 153, 458.
- [26] M. Rezaei, S. Li, S. Huang, K. V. Agrawal, *J. Membr. Sci.* **2020**, 612, 118406.
- [27] X. Li, W. Cai, J. An, S. Kim, J. Nah, D. Yang, R. Piner, A. Velamakanni, I. Jung, E. Tutuc, S. K. Banerjee, L. Colombo, R. S. Ruoff, *Science* **2009**, 324, 1312.
- [28] M. M. Lucchese, F. Stavale, E. H. M. Ferreira, C. Vilani, M. V. O. Moutinho, R. B. Capaz, C. A. Achete, A. Jorio, *Carbon* **2010**, 48, 1592.
- [29] L. G. Cançado, A. Jorio, E. H. M. Ferreira, F. Stavale, C. A. Achete, R. B. Capaz, M. V. O. Moutinho, A. Lombardo, T. S. Kulmala, A. C. Ferrari, *Nano Lett.* **2011**, 11, 3190.

- [30] Q. Yuan, Z. Xu, B. I. Yakobson, F. Ding, *Phys. Rev. Lett.* **2012**, *108*, 245505.
- [31] H.-T. Chin, J.-J. Lee, M. Hofmann, Y.-P. Hsieh, *Sci. Rep.* **2018**, *8*, 4046.
- [32] B. Bekdüz, Y. Beckmann, J. Meier, J. Rest, W. Mertin, G. Bacher, *Nanotechnology* **2017**, *28*, 185601.
- [33] J.-Y. Hwang, C.-C. Kuo, L.-C. Chen, K.-H. Chen, *Nanotechnology* **2010**, *21*, 465705.
- [34] P. R. Kidambi, G. D. Nguyen, S. Zhang, Q. Chen, J. Kong, J. Warner, A.-P. Li, R. Karnik, *Adv. Mater.* **2018**, *30*, 1804977.
- [35] Y. Hao, M. S. Bharathi, L. Wang, Y. Liu, H. Chen, S. Nie, X. Wang, H. Chou, C. Tan, B. Fallahazad, H. Ramanarayan, C. W. Magnuson, E. Tutuc, B. I. Yakobson, K. F. McCarty, Y.-W. Zhang, P. Kim, J. Hone, L. Colombo, R. S. Ruoff, *Science* **2013**, *342*, 720.
- [36] X. Xu, Z. Zhang, L. Qiu, J. Zhuang, L. Zhang, H. Wang, C. Liao, H. Song, R. Qiao, P. Gao, Z. Hu, L. Liao, Z. Liao, D. Yu, E. Wang, F. Ding, H. Peng, K. Liu, *Nat. Nanotechnol.* **2016**, *11*, 930.
- [37] W. Guo, B. Wu, S. Wang, Y. Liu, *ACS Nano* **2018**, *12*, 1778.
- [38] C. Shen, Y. Jia, X. Yan, W. Zhang, Y. Li, F. Qing, X. Li, *Carbon* **2018**, *127*, 676.
- [39] S. Choubak, M. Biron, P. L. Levesque, R. Martel, P. Desjardins, *J. Phys. Chem. Lett.* **2013**, *4*, 1100.
- [40] T. Niu, M. Zhou, J. Zhang, Y. Feng, W. Chen, *J. Am. Chem. Soc.* **2013**, *135*, 8409.
- [41] J. Zhang, Z. Wang, T. Niu, S. Wang, Z. Li, W. Chen, *Sci. Rep.* **2014**, *4*, 4431.
- [42] A. Eckmann, A. Felten, A. Mishchenko, L. Britnell, R. Krupke, K. S. Novoselov, C. Casiraghi, *Nano Lett.* **2012**, *12*, 3925.
- [43] A. T. Rodriguez, X. Li, J. Wang, W. A. Steen, H. Fan, *Adv. Funct. Mater.* **2007**, *17*, 2710.
- [44] R. W. Baker, *Membrane Technology and Applications*, John Wiley & Sons Ltd, Chichester **2004**.
- [45] J. Schrier, *J. Phys. Chem. Lett.* **2010**, *1*, 2284.
- [46] C. A. Scholes, U. K. Ghosh, *Membranes* **2017**, *7*, 9.
- [47] Z. Yuan, R. P. Misra, A. G. Rajan, M. S. Strano, D. Blankschtein, *ACS Nano* **2019**, *13*, 11809.
- [48] K. V. Agrawal, J. D. Benck, Z. Yuan, R. P. Misra, A. G. Rajan, Y. Eatmon, S. Kale, X. S. Chu, D. O. Li, C. Gong, J. Warner, Q. H. Wang, D. Blankschtein, M. S. Strano, *J. Phys. Chem. C* **2017**, *121*, 14312.
- [49] J. D. Thomsen, J. Kling, D. M. A. Mackenzie, P. Bøggild, T. J. Booth, *ACS Nano* **2019**, *13*, 2281.
- [50] Z. Yuan, A. G. Rajan, G. He, R. P. Misra, M. S. Strano, D. Blankschtein, *ACS Nano* **2021**, *15*, 1727.
- [51] Z. Li, Y. Wang, A. Kozbial, G. Shenoy, F. Zhou, R. McGinley, P. Ireland, B. Morganstein, A. Kunkel, S. P. Surwade, L. Li, H. Liu, *Nat. Mater.* **2013**, *12*, 925.
- [52] A. Kozbial, F. Zhou, Z. Li, H. Liu, L. Li, *Acc. Chem. Res.* **2016**, *49*, 2765.
- [53] A. G. Rajan, K. S. Silmore, J. Swett, A. W. Robertson, J. H. Warner, D. Blankschtein, M. S. Strano, *Nat. Mater.* **2019**, *18*, 129.
- [54] S. Huang, S. Li, L. F. Villalobos, M. Dakhchoune, M. Micari, D. J. Babu, M. T. Vahdat, M. Mensi, E. Oveisi, K. V. Agrawal, *Sci. Adv.* **2021**, *7*, eabf0116.
- [55] B. Wang, N. Hu, H. Wang, Y. Zheng, R. Zhou, *J. Mater. Chem. A* **2015**, *3*, 12205.
- [56] C. Zhou, C. Yuan, Y. Zhu, J. Caro, A. Huang, *J. Membr. Sci.* **2015**, *494*, 174.
- [57] N. Kosinov, C. Auffret, V. G. P. Sripathi, C. Gücüyener, J. Gascon, F. Kapteijn, E. J. M. Hensen, *Microporous Mesoporous Mater.* **2014**, *197*, 268.
- [58] S. Himeno, T. Tomita, K. Suzuki, K. Nakayama, K. Yajima, S. Yoshida, *Ind. Eng. Chem. Res.* **2007**, *46*, 6989.
- [59] A. Huang, N. Wang, J. Caro, *Microporous Mesoporous Mater.* **2012**, *164*, 294.
- [60] K. Kida, Y. Maeta, K. Yogo, *Sep. Purif. Technol.* **2018**, *197*, 116.
- [61] F. Zhang, X. Zou, X. Gao, S. Fan, F. Sun, H. Ren, G. Zhu, *Adv. Funct. Mater.* **2012**, *22*, 3583.
- [62] Z. Kang, M. Xue, L. Fan, L. Huang, L. Guo, G. Wei, B. Chen, S. Qiu, *Energy Environ. Sci.* **2014**, *7*, 4053.
- [63] P. Nian, Y. Li, X. Zhang, Y. Cao, H. Liu, X. Zhang, *ACS Appl. Mater. Interfaces* **2018**, *10*, 4151.
- [64] A. Huang, W. Dou, J. Caro, *J. Am. Chem. Soc.* **2010**, *132*, 15562.
- [65] A. Huang, Q. Liu, N. Wang, Y. Zhu, J. Caro, *J. Am. Chem. Soc.* **2014**, *136*, 14686.
- [66] H. Guo, G. Zhu, I. J. Hewitt, S. Qiu, *J. Am. Chem. Soc.* **2009**, *131*, 1646.
- [67] H. W. Kim, H. W. Yoon, S.-M. Yoon, B. M. Yoo, B. K. Ahn, Y. H. Cho, H. J. Shin, H. Yang, U. Paik, S. Kwon, J.-Y. Choi, H. B. Park, *Science* **2013**, *342*, 91.
- [68] J. Yang, D. Gong, G. Li, G. Zeng, Q. Wang, Y. Zhang, G. Liu, P. Wu, E. Vovk, Z. Peng, X. Zhou, Y. Yang, Z. Liu, Y. Sun, *Adv. Mater.* **2018**, *30*, 1705775.
- [69] A. K. Itta, H.-H. Tseng, M.-Y. Wey, *J. Membr. Sci.* **2011**, *372*, 387.
- [70] H.-C. Lee, M. Monji, D. Parsley, M. Sahimi, P. Liu, F. Eglolfopoulos, T. Tsotsis, *Ind. Eng. Chem. Res.* **2013**, *52*, 1122.
- [71] H.-H. Tseng, C.-T. Wang, G.-L. Zhuang, P. Uchytel, J. Reznickova, K. Setnickova, *J. Membr. Sci.* **2016**, *510*, 391.
- [72] M. A. L. Tanco, J. A. Medrano, V. Cechetto, F. Gallucci, D. A. P. Tanaka, *Int. J. Hydrogen Energy* **2020**, *46*, 19758.
- [73] D. Lee, L. Zhang, S. T. Oyama, S. Niu, R. F. Saraf, *J. Membr. Sci.* **2004**, *231*, 117.
- [74] R. M. de Vos, H. Verweij, *Science* **1998**, *279*, 1710.
- [75] S.-J. Ahn, A. Takagaki, T. Sugawara, R. Kikuchi, S. T. Oyama, *J. Membr. Sci.* **2017**, *526*, 409.
- [76] Y. Gu, P. Hacırlıoğlu, S. T. Oyama, *J. Membr. Sci.* **2008**, *310*, 28.
- [77] S.-J. Ahn, G.-N. Yun, A. Takagaki, R. Kikuchi, S. T. Oyama, *J. Membr. Sci.* **2018**, *550*, 1.
- [78] H. F. Qureshi, A. Nijmeijer, L. Winnubst, *J. Membr. Sci.* **2013**, *446*, 19.
- [79] R. S. A. de Lange, J. H. A. Hekkink, K. Keizer, A. J. Burggraaf, *Microporous Mater.* **1995**, *4*, 169.
- [80] H. L. Castricum, H. F. Qureshi, A. Nijmeijer, L. Winnubst, *J. Membr. Sci.* **2015**, *488*, 121.